SSC24-WVIII-03

# Omnidirectional Radio Interferometry
# Using Deployable Tensegrity Array Antenna Satellite

Yosuke Tanabe, Tsukasa Funane, Hisatoshi Kimura, Makoto Ito, Koichi Watanabe
Hitachi, Ltd. Research & Development Group
1-280 Higashi-koigakubo, Kokubunji-shi, Tokyo, 185-8601 Japan; +81-80-7738-5101
yosuke.tanabe.pb@hitachi.com

Yasuyuki Miyazaki
Japan Aerospace Exploration Agency
3-1-1 Yoshinodai, Chuo-ku, Sagamihara-shi, Kanagawa, 252-5210 Japan; +81-70-1170-2801
miyazaki.yasuyuki@jaxa.jp

Shinichi Nakasuka
The University of Tokyo
7-3-1 Hongo, Bunkyo-ku, Tokyo, 113-8656 Japan; +81-3-5841-6590
nakasuka@space.t.u-tokyo.ac.jp

## ABSTRACT

We propose a method of omnidirectional radio interferometry in space using a three-dimensional tensegrity array antenna deployed from a small satellite. Tensegrity means a stable and self-equilibrating structure based on the balance of compressive and tensile forces between compression and tension members. The advantages of the tensegrity structure are that it is lightweight and can be stored compactly, reducing launch costs and enabling deployment in orbit. This structure is therefore attracting interest for various applications such as space antennas, starshades, and planetary exploration. In this study, we investigated a tensegrity array antenna that can be deployed from small satellites as a platform for a space-based radio interferometer. This is an attempt to advance the proposed method of omnidirectional radio interferometry to enable us to configure sensor pairs with multiple baseline lengths and arbitrarily change the baseline vectors with respect to the observation target by rotating the satellite. With a wide field of view, the tensegrity array antenna employing this method can serve a variety of applications, including science and space situational awareness.

The tensegrity array antenna deploys bars and thin films as compression and tension members of the tensegrity structure to form a tensegrity icosahedron with an outer shape more than twice as large as that of a small satellite in storage. The bars are used as pole antennas and the thin films as patch antennas to form a three-dimensional array antenna with thirteen axes of rotational symmetry. We propose the method to estimate the omnidirectional distribution of the scalar sources by measuring the interference between the antenna pairs while rotating the tensegrity array antenna around the rotational symmetry axis.

We present the configuration of the tensegrity array antenna as well as its deployment. We also propose an estimation method for the omnidirectional distribution of the scalar sources by rotational interferometry using the spherical harmonic expansion. We report the verification results of this estimation method using the similarity rule between electromagnetics and acoustics. For the verification, we constructed a six-channel array microphone and measured uncorrelated one-third octave bandpass noise (center frequencies of 1 k and 2 kHz, corresponding to 0.9 G and 1.8 GHz in radio-frequency conversion) emitted from multiple directions in an anechoic chamber by rotating the array microphone. The results indicate the ability to separate sources arriving simultaneously from multiple directions at 10 dB signal-to-noise ratio. This was achieved with the theoretical resolution of the interferometer. Finally, we discuss the development challenges and future works.

## INTRODUCTION

Since the early 2000s, the space industry has tended to move towards private sector-led space development, with many ventures being established. As a result of the efforts of various countries and these ventures, a large number of satellites have been deployed in low Earth orbit for communication[1], Earth observation[2] and SIGINT[3] (Signal Intelligence) purposes, and the Earth's orbit is becoming overcrowded, with the total number of spacecraft and debris reaching 27,942 in April 2024[4].

To ensure the safe and continuous operation of satellites in such crowded conditions, space situational awareness (SSA) technology is essential to monitor obstacles stagnating in the omni-direction for space traffic management (STM). Conventional SSA is mainly based on ground-based observations using radar or optical telescopes[5], but the status of obstacles that are out of sight of ground stations cannot be constantly monitored.

Therefore, this paper proposes an estimation method for future SSA that locates objects around a satellite by omnidirectional radio interferometry using a three-dimensional (3D) tensegrity array antenna deployed from a small satellite. The proposed method is intended for observation of active objects emitting radio waves but may be applicable to non-active objects with a combination of radar technologies.

## TENSEGRITY ARRAY ANTENNA

This section presents the tensegrity array antenna using a tensegrity structure suitable for omnidirectional interferometry that we will propose later. Tensegrity means a stable and self-equilibrating structure based on the balance of compressive and tensile forces between compression and tension members[6]. The icosahedral tensegrity array antenna is shown in Fig. 1.

The left side of Fig. 1 shows an overview of the array antenna structure, which consists of 6 compression members used as the pole antennas, 24 tension members used as cables and thin films, and 12 nodes connecting the compression and tension members. In general, a stable structure must satisfy the following extended Maxwell's formula[7] as

$$Num. of\ compression\ members\ +\ Num. of\ tension\ members\ \geq\ 3 \times Num. of\ nodes - 6. \qquad (1)$$

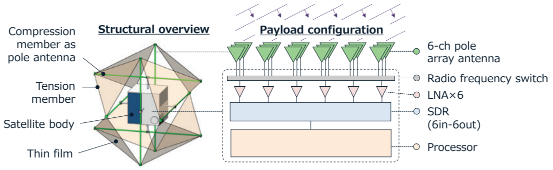

**Fig. 1 Overview of Tensegrity Array Antenna and Payload Configuration**

Since the left and right sides of Eq. (1) are equal, the tensegrity array antenna can have a lightweight and stable structure with a minimal number of components.

The right side of Fig. 1 shows an example of a payload configuration. Six bars are used as pole antennas to form a six-channel 3D array antenna. The received signals from the antennas are amplified using low noise amplifier (LNA), acquired by software defined radio (SDR), then processed using a processor to execute omnidirectional interferometry as described in the next section.

In interferometry, the relative position of the observation target and antenna pair must be varied to observe data at different baselines, such as very large baseline interferometry (VLBI) with radio telescopes using the Earth's rotation[8]. Since it is placed in satellite-centered symmetry, the tensegrity array antenna has 13 rotational symmetry axes, where $C_n$ $(n \in \mathbb{N}^+)$ represents an axis of $360^{\circ}/n$ rotation, as shown in Fig. 2. Including the identity transformation $E$, the tensegrity array antenna can execute rotational interferometry with total of 14 operations $\boldsymbol{O} = \{4C_3, 3C_4, 6C_2, E\}$.

The on-orbit deployment of the tensegrity array antenna is shown in Fig. 3, which involves using an extensible boom for the compression member and rotating double-fold origami-based membrane as the thin-film structure[9].

By extending the boom in the direction of the red arrow, the origami structure stored at the edge of the satellite rotates and unfolds to form an equilateral triangular thin film. Because the deployed outer shape is more than

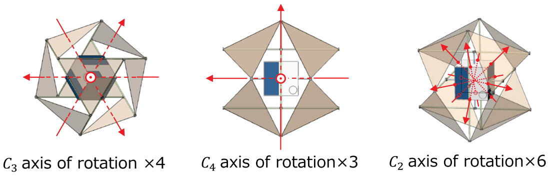

**Fig. 2 Rotational Axes of Tensegrity Satellite**

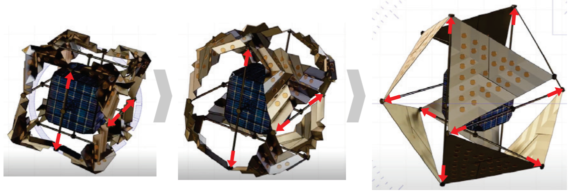

**Fig. 3 On-orbit Deployment**

twice the size of the small satellite in storage, patch antennas and solar cells may be mounted on the film to deploy a highly functional large membrane around the satellite.

## OMNIDIRETIONAL INTERFEROMETRY

This section describes the proposed method of omnidirectional radio interferometry using the tensegrity array antenna.

### *Source Representation by Spherical Harmonics*

In a coordinate system centered on a spacecraft equipped with a 3D tensegrity array antenna, we denote the omnidirectional scalar source brightness at $k = |\boldsymbol{k}|$ as $B(\Omega_k)$, where $\boldsymbol{k}$ is the wavenumber vector, $\Omega_k = (\theta_k, \phi_k)$ is the solid angle and $\theta_k, \phi_k$ are the elevation and azimuth angles, respectively. The wavenumber-domain expression of the source brightness, visibility $\mathcal{V}$, is given by

$$\mathcal{V}(\boldsymbol{r}, k) = \int B(\Omega_k) \exp(-i\boldsymbol{k} \cdot \boldsymbol{r}) d\Omega_k, \tag{2}$$

where $\boldsymbol{r}$ is the position vector. Using spherical harmonics $Y_{lm}$ ($l$ and $m$ are the polar and azimuthal quantal numbers, respectively), the visibility $\mathcal{V}(\boldsymbol{r}, k)$, $B(\Omega_k)$, and term $\exp(-i\boldsymbol{k} \cdot \boldsymbol{r})$ are respectively expressed as

$$\mathcal{V}(\boldsymbol{r}, k) = \sum_{l=0}^{\infty} \sum_{m=-l}^{l} v_{lm} j_l(kr) Y_{lm}(\theta_r, \phi_r), \tag{3}$$

$$B(\Omega_k) = \sum_{l=0}^{\infty} \sum_{m=-l}^{l} b_{lm} Y_{lm}(\Omega_k) \tag{4}$$

and

$$\exp(-i\boldsymbol{k} \cdot \boldsymbol{r}) = 4\pi \sum_{l=0}^{\infty} \sum_{m=-l}^{l} (-i)^l j_l(kr) Y_{lm}(\theta_r, \phi_r) Y_{lm}^*(\Omega_k). \tag{5}$$

In Eq. (3), $v_{lm}$, $r = |\boldsymbol{r}|$ and $j_l(kr)$ are the expansion coefficient of visibility, radius and spherical Bessel functions of the first kind, respectively. In Eq. (4), $b_{lm}$ is the expansion coefficient of brightness.

Substituting Eqs. (3), (4) and (5) into Eq. (2) yields the relationship between $v_{lm}$ and $b_{lm}$ as follows[10]:

$$v_{lm} = 4\pi(-i)^l b_{lm}. \tag{6}$$

### *Visibility observations*

Visibility observations use interference fringes, which are obtained by receiving signals emitted from the same radio source with a pair of antennas and interfering with those signals.

Fig. 4 (a) shows an antenna pair Ant$_i$ and Ant$_j$ arranged on baseline vector $\boldsymbol{D}_{ij}(r, \theta, \phi)$ ($r, \theta, \phi$ are the radius, elevation and azimuth angle, respectively) obtained from the difference in the center coordinates between Ant$_i$ and Ant$_j$. The observed radio source at wavelength $\lambda$ is assumed in direction $\boldsymbol{s}$, viewed from the center of the array antenna.

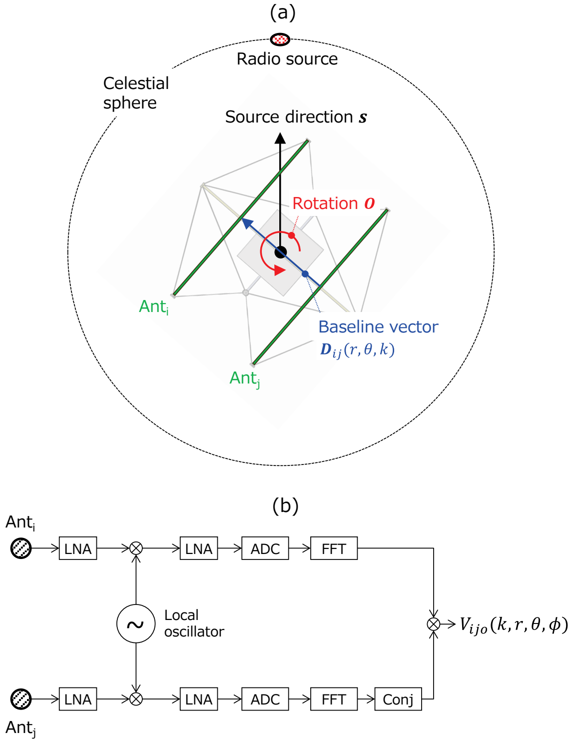

**Fig. 4 (a) Schematic of Rotational Interferometry of Antenna Pairs Separated by Distance *D*, (b) Signal-processing Flowchart for Visibility Observation**

The $\boldsymbol{D}_{ij}$ is time varying due to the rotational operation $\boldsymbol{O}$ of the array antenna. If the spacing of the antenna pair is large enough with respect to $\lambda$, periods for Fourier analysis can be observed in the interference fringes obtained from receiving signals with the antenna pair during small rotational operation $\Delta\boldsymbol{O}$.

Fig. 4 (b) shows a flowchart for visibility observation from signals received under the small rotational operation $\Delta\boldsymbol{O}_o$ in a certain time interval $\Delta t_o$. Signals from Ant$_i$ and Ant$_j$ are first amplified with an LNA and converted to the appropriate frequency with the local oscillator. The signals are then amplified again with the LNA and converted from analog to digital signals with an analog-to-digital converter (ADC). Finally, the samples at $\Delta\boldsymbol{O}_o$ are transformed to the frequency domain by fast Fourier transform (FFT) and the cross-spectrum between Ant$_i$ and Ant$_j$ is calculated to obtain visibility $V_{ijo}(k,r,\theta,\phi)$.

Assuming that the number of antennas is $N$ and total number of $\Delta\boldsymbol{O}_o$ is $M$, $v_{lm}$ can be estimated as

$$v_{lm} \sim \frac{2k^2}{\pi}\sum_{o=1}^{M}\sum_{i=1}^{N}\sum_{j\neq i,j>i}^{N} V_{ijo}(k,r,\theta,\phi)\, j_l(kr)\, Y_{lm}^{*}(\theta,\phi). \qquad (7)$$

Substituting the above into Eq. (6) gives $b_{lm}$; thus $B(\Omega_k)$ can be reconstructed from Eq. (4). Note that the theoretical angular resolution $\vartheta_{min}$ is given by the following relationship between $\lambda$ and baseline length $|\boldsymbol{D}_{ij}|$ on the basis on the theory of interferometry[8].

$$\vartheta_{min} \approx \lambda/|\boldsymbol{D}_{ij}| \qquad (8)$$

## VALIDATION

This section reports the verification results of the proposed method using the similarity rule between electromagnetics and acoustics.

### *Similarity between Electromagnetics and Acoustics*

An electromagnetic wave is a transverse wave caused by the interaction of the electric and magnetic fields, while an acoustic wave is a longitudinal wave caused by the propagation of compression in a medium. However, there is duality and similarity in the governing equations of both, and it is known that physical phenomena such as reflection, refraction and interference, which the proposed estimation method uses, exhibit similar characteristics[11]. Therefore, we verified the proposed method through acoustic experiments using the electromagnetics-acoustics similarity law. To evaluate electromagnetic interference phenomena acoustically, the following relationship[12] must be satisfied.

$$\frac{LF}{c} = \frac{L'F'}{c'}, \qquad (9)$$

where $c$ and $c'$ are the speed of light and sound, $L$ and $L'$ are the representative array lengths of the antenna and microphone, and $F$ and $F'$ are the target frequency of the electromagnetic and acoustic waves, respectively. Table 1 shows the electromagnetic – acoustic similarity rule used in this paper.

We set $c$ = 3.0×10$^8$ m/s and $c'$ = 340 m/s. The $L$ = $L'$ = 0.44 m is the distance between the opposing sensors in the *x*-, *y*-, and *z*-axes as shown in Fig. 2(a). The $F'$s in these acoustic experiments were 1 k and 2 kHz, and by substituting them into Eq. (9), the corresponding $F$s were 0.88 G and 1.8 GHz.

### *Array-microphone Arrangement and Coordinates*

Fig. 5 (a) shows the configuration of a six-channel array microphone with omnidirectional microphones (JTS, CX-500) at the points indicated with red circles. As shown in Table 2, the microphones were placed at a distance of 0.44 m, which is the representative array length, from the origin in the *x*-, *y*-, and *z*-axes, respectively.

Fig. 5 (b) illustrates the definition of the spherical coordinate system used to indicate the position of the radio source on the virtual celestial sphere around the array.

### *Experimental Setup*

The experiments were conducted in an anechoic chamber with a controllable background noise level. Fig. 6 shows the anechoic chamber and the experimental setup. The six-channel array microphone mounted on a single-axis rotator (Thorlabs, HDR50) was placed in the center of the spherical 26-ch array loudspeaker[13] with a diameter of 3.25 m. The controller of the single-axis rotator (Thorlabs, BSC201) and analog-to-digital audio interface (Focusrite, Scarlett 18i20) for microphone-data acquisition were controlled with the same laptop PC. The rotation speed was set to $2\pi/36$ rad/s, and six channels of audio data were acquired simultaneously at a sampling frequency of 44,100 Hz for 36 s during one rotation of the array microphone.

**Table 1: Electromagnetic (EM) - acoustic Similarity Rule**

| | EM | Acoustics | Wavelength[m] |
|---|---|---|---|
| **Speed [m/s]** | $c$ = 3.0×10$^8$ | $c'$ = 340 | - |
| **Length [m]** | $L$ = 0.44 | $L'$ = 0.44 | - |
| **Frequency [Hz]** | $F$ = 8.8×10$^8$ | $F'$= 1,000 | $\lambda$ = 0.34 |
| | $F$ = 1.8×10$^9$ | $F'$= 2,000 | $\lambda$ = 0.17 |

**Table 2: Coordinates of Six-channel Microphone**

| Name | Coordinates | | |
|---|---|---|---|
| | ***x* [m]** | ***y* [m]** | ***z* [m]** |
| Mic$_1$ | 0.22 | 0 | 0 |
| Mic$_2$ | −0.22 | 0 | 0 |
| Mic$_3$ | 0 | 0.22 | 0 |
| Mic$_4$ | 0 | −0.22 | 0 |
| Mic$_5$ | 0 | 0 | 0.22 |
| Mic$_6$ | 0 | 0 | −0.22 |

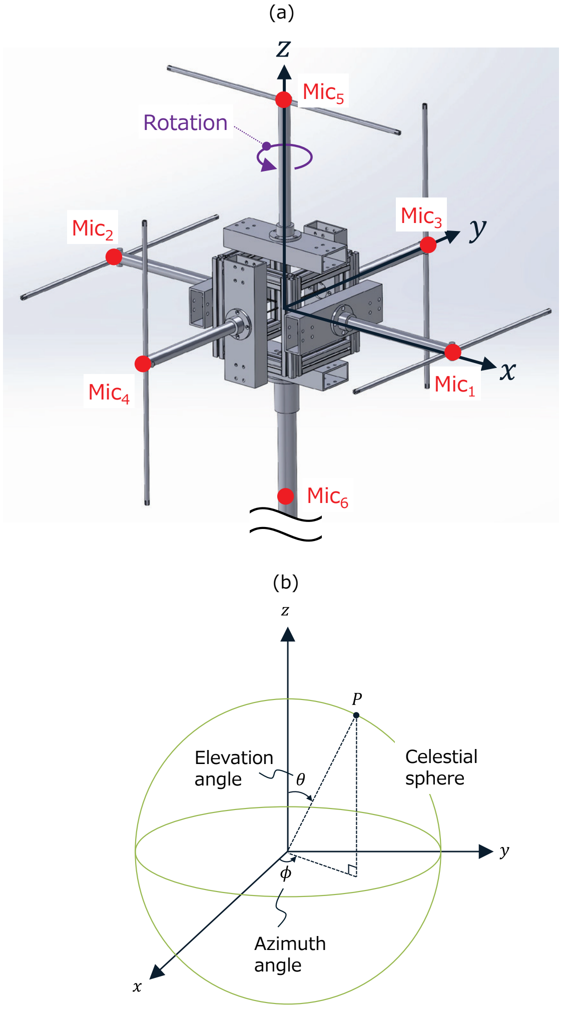

**Fig. 5 (a) Coordinate System for Experiments and Arrangement of Microphones in Array, (b) Polar Coordinate System for Representing Omnidirectional Distribution of Scalar Sources**

Fig. 7 shows the location and name of each loudspeaker (Genelec, 8320A) as viewed from $4\pi$ space, with the azimuth angle on the horizontal axis and elevation angle on the vertical axis.

Each loudspeaker can output an audio signal from the digital-to-analog interface controlled with a desktop PC placed outside the anechoic chamber. In the experiments, one-third octave bandpass noise with center frequencies of 1 k and 2 kHz was used as the signal source.

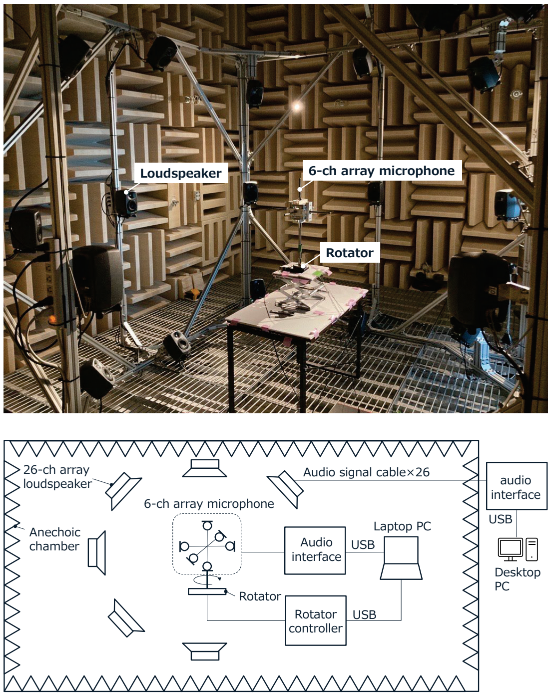

**Fig. 6 Experimental Setup in Anechoic Chamber**

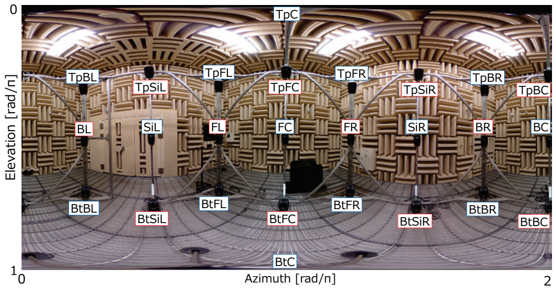

**Fig. 7 Loudspeaker Layout Viewed from $4\pi$ Space**

### *Results*

We present the results of two cases: one in which the signal is output from front right (FR) as a single source, and the other in which uncorrelated signals are output from side right (SiR) and bottom back right (BtBR) as multiple sources. Fig. 8 shows the $b_{lm}$ calculated with the proposed method with the maximum polar quantal number $l_{\max}$ of the spherical harmonics is 15.

In Fig. 8, the horizontal axis is the number of $b_{lm}$ ($\{l_{\max}+1\}^2 = 256$ coefficients in total) ordered from the lowest order of the polar quantal number as $(l,m) = (0,0),(1,-1),(1,0),(1,1),\ldots$. The vertical axis shows the $b_{lm}$ in dB, and the graph can be interpreted as a spectrum

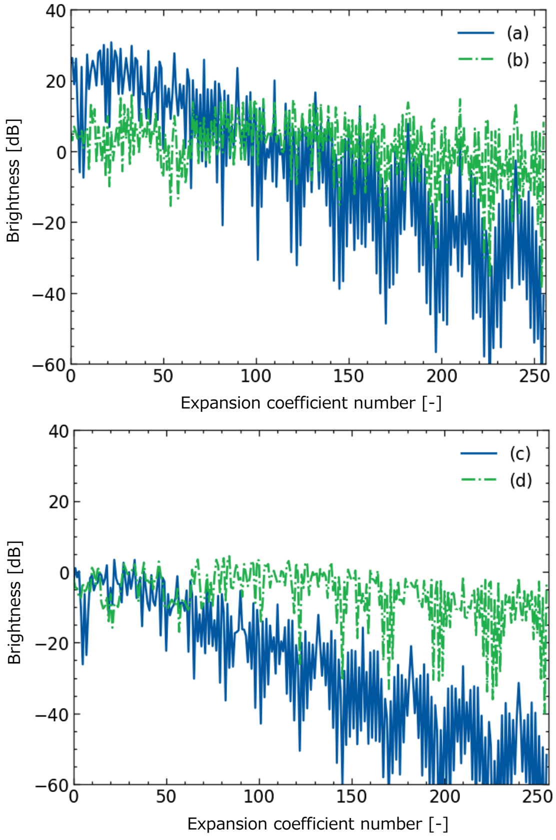

**Fig. 8 Measurement Results of Source $b_{lm}$ of (a) FR at 1 kHz, (b) FR at 2 kHz, (c) SiR and BtBR at 1 kHz, and (d) SiR and BtBR at 2 kHz**

of spherical harmonics. Comparing Fig. 8 (a) and (b), and comparing (c) and (d), we can see that the higher the target frequency, the greater the higher order components of $b_{lm}$. This may be because the angular resolution by interferometry is proportional to $\lambda$ as shown in Eq. (8), so that a higher order components of $b_{lm}$ is needed at 2 kHz, which is shorter $\lambda$ than 1 kHz, to represent the source location in detail. Next, the reconstructed results of the source localization from $b_{lm}$ and Eq. (4) with 400 azimuthal pixels and 200 elevation pixels are shown in Fig. 9.

Fig. 9 shows the normalized azimuth and elevation angles [rad/$\pi$] on the horizontal and vertical axes, respectively. The color map is the normalized source brightness displayed in the range of −3 to 0 dB, and the array loudspeaker image in Fig. 7 is superimposed so that the brightness distribution corresponds to the loudspeaker location.

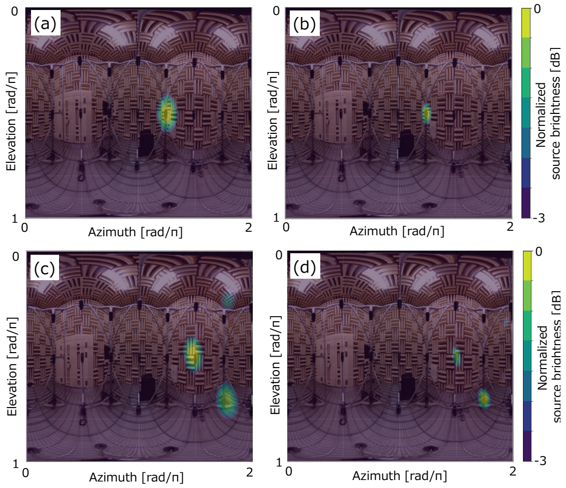

**Fig. 9 Results of Source Localization of (a) FR at 1 kHz, (b) FR at 2 kHz, (c) SiR and BtBR at 1 kHz, and (d) SiR and BtBR at 2 kHz**

Fig. 9 (a) and (b) show the source localization when the 1 k and 2 kHz signals were output from FR, respectively. Both results indicate that the maximum point of brightness coincides with the loudspeaker position. Comparing (a) and (b), the angular resolution improved at 2 kHz because the resolution of the interferometer is proportional to the $\lambda$ as shown in Eq. (8).

Fig. 9 (c) and (d) show the source localization when uncorrelated 1 k and 2 kHz signals were output from SiR and BtBr, respectively. These results also indicate that the maximum brightness point generally coincides with the loudspeaker position. However, spurious sources are observed near top back right (TpBR) and top back center (TpBC), indicating that accuracy may deteriorate with increasing field complexity.

We next obtained the 2D graphs of the azimuth and elevation angles at which the brightness is maximum in Fig. 9 (a) and (b), as shown in Fig. 10, for investigating angular resolution.

Fig. 10, (a1), (b1) and (a2), (b2) show the normalized brightness with respect to azimuth and elevation angles, respectively. The red vertical dotted line shows the theoretical angular resolution (0.25 rad/$\pi$ for (a1) and (a2), and 0.12 rad/$\pi$ for (b1) and (b2)) calculated using Eq. (8), while the green horizontal dashed line shows the half-power line representing the measured angular resolution. Both are in close agreement, indicating that

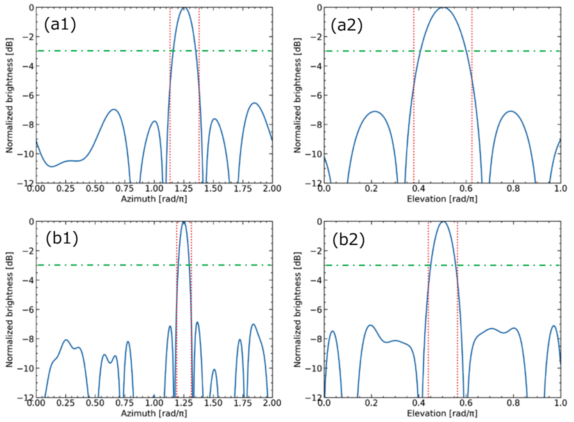

**Fig. 10 Angular Resolution of Source FR in (a1) Azimuth at 1 kHz, (a2) Elevation at 1 kHz, (b1) Azimuth at 2 kHz, and (b2) Elevation at 2 kHz**

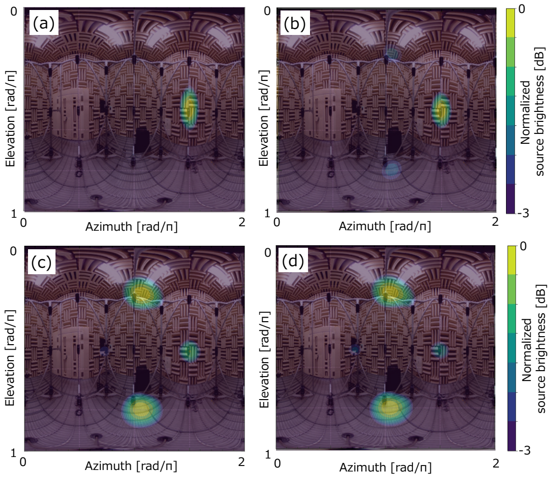

**Fig. 11 Results of 1 kHz Source Localization of SiR at SNR = a) 65 dB, b) 10 dB, c) 6 dB, and d) 4 dB**

the angular resolution of the proposed method can be estimated from Eq. (8).

Finally, we investigated the relationship between signal-to-noise ratio (SNR) and accuracy of source localization as shown in Fig. 11. We defined SNR as the intensity ratio of the target signal to the background noise at the center of the array microphone.

Fig. 11 shows the source-localization results when 1 kHz bandpass noise signal was output from SiR as the target signal and uncorrelated signals with the same bandwidth from other 25ch loudspeakers as the background noise. Fig. 11, (a) shows SNR = 65 dB without background noise, and (b), (c), and (d) show SNR = 10, 6, and 4 dB with background noise, respectively. As shown in Fig. 11 (b), spurious sources were observed near top front center (TpFC) and bottom front center (BtFC), but the highest brightness matched SiR, which is the target signal source. However, the spurious sources near TpFC and BtFC were larger than those near SiR for SNR = 6 and 4 dB, and the target source could not be identified.

To improve localization accuracy, it may be necessary to add different rotation axes to sample the variety of visibility and to increase $l_{\max}$ to reconstruct the complex field.

## FUTURE WORK

We conducted validation experiments using an array microphone equipped with an omnidirectional microphone based on the electromagnetic–acoustic similarity rule. However, to observe distant obstacles using an array antenna for SSA, it is necessary to narrow the dispersion pattern of the antenna to increase the gain. Since the proposed method uses the array antenna around the satellite, the interferometric performance needs to be evaluated considering the diffraction effect of the radio waves by the satellite's enclosure.

Fig. 12 shows the simulation results of a radiation pattern from a directional (dipole) antenna deployed around a small satellite.

The satellite enclosure, modeled as a 1.5-mm thick hollow aluminum box, shields the radio waves and prevents them from reaching the opposing antenna. Consequently, interferometry with pairs of opposing antennas that can form the longest baseline cannot be executed, which would degrade the angular resolution of the observation. Therefore, future work is to study the performance of omnidirectional interferometry, including the effects of antenna directivity and satellite enclosures, to investigate feasible array antenna

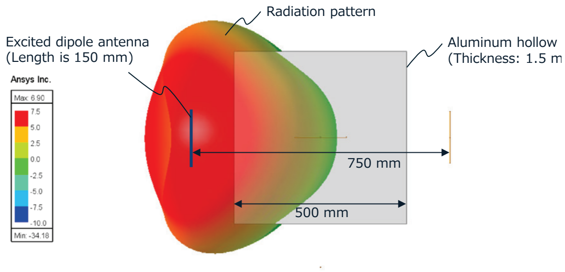

**Fig. 12 Simulation of the Effect of the Satellite Enclosure on the Radiation Pattern**

configurations. Other areas for future work include satellite system studies including deployment mechanism, and mission design.

## CONCLUSION

We have proposed the omnidirectional interferometry using tensegrity array antenna satellite for future SSA. We have discussed the concept of the icosahedron-shaped tensegrity array antenna satellite with six compression members as a 3D array antenna suitable for omnidirectional measurements while rotating using the symmetry of the structure. We have also proposed a method for estimating the location of scalar radio sources around satellites on the basis of interference fringes obtained from antenna pairs using spherical harmonics. For a proof-of-principle study, we have conducted acoustic experiment in an anechoic chamber to demonstrate the ability to separate sources arriving simultaneously from multiple directions with SNR of 10 dB. Although the configuration of the feasible tensegrity array antenna around the satellite remains for future work, the proposed method would be useful for future SSA to observe obstacles in all directions for STM.

### *Acknowledgments*

The authors would like to express their sincere thanks to Shingo Seki, Yumiho Takeuchi, and Takuya Aoki for their cooperation in the experiments and to Takumi Obuchi, Tsutomu Okazaki, and Nobuhiro Ishimaru for continuous discussions.

### *References*

1. McDowell, J. C., “The Low Earth Orbit Satellite Population and Impacts of the SpaceX Starlink Constellation,” The Astrophysical Journal Letters, vol. 892, 2020.
2. Orzel, K., Fujimaru, S., Obata, T., Imaizumi, T., and M. Arai, “StriX-α SAR Satellite: Demonstration of Observation Modes and Initial Calibration Results,” 14th European Conference on Synthetic Aperture Radar, 2022.
3. Sarda, K., CaJacob, D., Orr, N., and R. Zee, “Making the Invisible Visible: Precision RF-emitter Geolocation from Space by the Hawkeye 360 Pathfinder Mission,” The 32nd Annual AIAA/USU Conference on Small Satellites, 2018.
4. Cowardin, H., “Orbital Debris Quarterly News, April 2024,” Orbital Debris Quarterly News, vol. 28, 2024.
5. Lal, B., Balakrishnan, A., Caldwell, B. M., Buenconsejo, R. S., and S. A. Carioscia, Global Trends in Space Situational Awareness (SSA) and Space Traffic Management (STM), Institute for Defense Analyses, 2018.
6. Skelton, R. E. and M. C. De Oliveira, Tensegrity systems vol. 1: Springer, 2009.
7. Calladine, C. R., “Buckminster Fuller's Tensegrity Structures and Clerk Maxwell's Rules for the Construction of Stiff Frames,” International journal of solids and structures, vol. 14, pp. 161-172, 1978.
8. Bradt, H., Astronomy methods: A Physical Approach to Astronomical Observations, Cambridge University Press, 2004.
9. Miyazaki, Y., “Deployable Techniques for Small Satellites, ” Proceedings of the IEEE, vol. 106, pp. 471-483, 2018.
10. Carozzi, T., “Imaging on a Sphere with Interferometers: the Spherical Wave Harmonic Transform,” Monthly Notices of the Royal Astronomical Society: Letters, vol. 451, pp. L6-L10, 2015.
11. Staelin, D., 6.013 Electromagnetics and Applications, Massachusetts Institute of Technology: MIT OpenCouseWare, https://ocw.mit.edu/. License: Creative Commons BY-NC-SA, Spring 2009.
12. Emori, R. I. and D. J. Schuring, Scale Models in Engineering, Pergamon, 1977.
13. Tanabe, Y., Yamauchi, G., Marui, A., and T. Kamekawa, “Tesseral Array for Group Based Spatial Audio Capture and Synthesis,” 2020 AES International Conference on Audio for Virtual and Augmented Reality, 2020.